Phase diagram of the weak-magnetic-field quantum Hall transition quantified from classical percolation

M. Ortuño,[1] A. M. Somoza,[1] V. V. Mkhitaryan,[2] and M. E. Raikh[2]
[1]*Departamento de Física-CIOyN, Universidad de Murcia, Murcia ES-30071, Spain*
[2]*Department of Physics, University of Utah, Salt Lake City, Utah 84112, USA*
(Received 25 May 2011; published 7 October 2011)

We consider magnetotransport in high-mobility two-dimensional electron gas $\sigma_{xx} \gg 1$ in a nonquantizing magnetic field. We employ a weakly chiral network model to test numerically the prediction of the scaling theory that the transition from an Anderson to a quantum Hall insulator takes place when the Drude value of the nondiagonal conductivity σ_{xy} is equal to $1/2$ (in the units of e^2/h). The weaker the magnetic field, the harder it is to locate a delocalization transition using quantum simulations. The main idea of this study is that the *position* of the transition does not change when a strong *local* inhomogeneity is introduced. Since the strong inhomogeneity suppresses interference, transport reduces to classical percolation. We show that the corresponding percolation problem is bond percolation over two sublattices coupled to each other by random bonds. Simulation of this percolation allows us to access the domain of very weak magnetic fields. Simulation results confirm the criterion $\sigma_{xy} = 1/2$ for values $\sigma_{xx} \sim 10$, where they agree with earlier quantum simulation results. However, for larger σ_{xx}, we find that the transition boundary is described by $\sigma_{xy} \sim \sigma_{xx}^{\kappa}$ with $\kappa \approx 0.5$, i.e., the transition takes place at higher magnetic fields. The strong inhomogeneity limit of magnetotransport in the presence of a random magnetic field, pertinent to composite fermions, corresponds to a different percolation problem. In this limit, we find for the delocalization transition boundary $\sigma_{xy} \sim \sigma_{xx}^{0.6}$.

DOI: 10.1103/PhysRevB.84.165314 PACS number(s): 72.15.Rn, 73.20.Fz, 73.43.−f

I. INTRODUCTION

Anderson localization is a *single-particle* phenomenon. Nevertheless, the scaling theory of localization,[1] which yields a profound prediction, i.e., full localization of all states in two dimensions, was formulated in terms of conductivity of *electron gas* σ. Similarly, the extension[2] of the two-dimensional (2D) scaling theory to a finite magnetic field is formulated in terms of components σ_{xx} and σ_{xy} of the conductivity tensor of electron gas. Scaling equations describing the evolution of these components with the sample size L have the form

$$\frac{\partial \sigma_{xx}}{\partial \ln L} = -\frac{1}{2\pi^2 \sigma_{xx}} - \sigma_{xx}^2 \mathcal{D} e^{-2\pi\sigma_{xx}} \cos(2\pi\sigma_{xy}), \tag{1}$$

$$\frac{\partial \sigma_{xy}}{\partial \ln L} = -\sigma_{xx}^2 \mathcal{D} e^{-2\pi\sigma_{xx}} \sin(2\pi\sigma_{xy}), \tag{2}$$

where $\mathcal{D}$ is a dimensionless constant. Drude values of σ_{xx} and σ_{xy} at size L of the order of mean-free path l are given by

$$\sigma_{xx}\big|_{L\sim l} = \frac{\sigma_0}{1+(\omega_c\tau)^2}, \qquad \sigma_{xy}\big|_{L\sim l} = \frac{\sigma_0\,(\omega_c\tau)}{1+(\omega_c\tau)^2}, \tag{3}$$

where $\sigma_0 = k_F l$, k_F is the Fermi wave vector, ω_c is the cyclotron frequency, and τ is the scattering time. These values serve as initial conditions to Eqs. (1) and (2). Fixed points $\sigma_{xy} = n + 1/2$, at which σ_{xx} is finite, determine the energies of delocalized states

$$E_n = \hbar\omega_c \left(n + \frac{1}{2}\right)\left[1 + \frac{1}{(\omega_c\tau)^2}\right]. \tag{4}$$

The most nontrivial consequence of Eq. (4) is that it predicts levitation of delocalized states in weak magnetic fields $\omega_c\tau \ll 1$ [see Fig. 1(a)]. In such fields, it takes the form $E_n = (n+\frac{1}{2})\hbar/\omega_c\tau^2$. In physical terms, this means that a high-mobility electron gas with zero-field Drude conductivity $\sigma_{xx} = E_F\tau/\hbar \gg 1$ exhibits a very strong sensitivity to a weak magnetic field

$$\omega_c\tau \sim \hbar/E_F\tau \tag{5}$$

as the temperature is decreased and quantum interference effects become important. The phenomenon of levitation was predicted by Khmelnitskii[3] even before Eqs. (1) and (2) were put forward (see also Ref. 4). Subsequently, it was observed experimentally by several groups.[5–12] This discovery initiated a number of theoretical studies,[13–29] which, however, did not demonstrate levitation in a truly weak-field limit $\omega_c\tau \ll 1$.

A. Physical interpretation of Eq. (1)

The starting point in derivation of scaling equations (1) and (2) was a σ model with topological term.[2] It is desirable to understand physical processes underlying these equations. The first term in Eq. (1) comes from Aharonov-Bohm *phase* action of the magnetic field. It describes that two paths corresponding to the same scatterers but different sequences of scattering events interfere even in the presence of the Aharonov-Bohm phases. The interpretation of the second term in Eq. (1) is transparent in the limit of classically strong magnetic field $\omega_c\tau > 1$, where $\cos(2\pi\sigma_{xy})$ assumes the form $\cos(2\pi E_F/\hbar\omega_c)$, which is simply the field-induced modulation of the density of states. The origin of modulation is the emergence of Landau levels. On the other hand, Landau levels reflect the *orbital* action of the magnetic field, i.e., the fact that, with a certain probability, an electron can complete a Larmour circle with radius R_L without being scattered away by disorder. Thus, the interpretation of the right-hand side of Eq. (1) is that the phase and orbital actions of the magnetic field compete with each other.

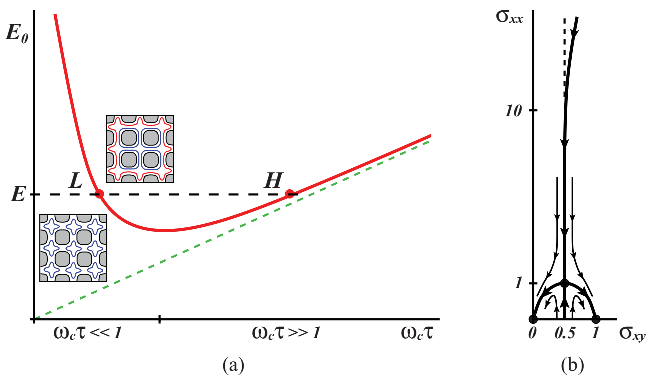

FIG. 1. (Color online) (a) Energy position of delocalized state E_0 versus magnetic field ω_c as predicted by Eq. (4). The curve $E_0(\omega_c)$ separates the phases with quantized Hall conductivities $\sigma_{xy} = 0$ and $\sigma_{xy} = 1$. Cartoons illustrate electron trajectories with restricted geometry in both phases; the red (gray) edge state is present in the upper cartoon and absent in the lower cartoon. (b) The predicted modification of the form of the flow diagram (Ref. 3) is illustrated schematically.

Unlike strong fields, the interpretation of the cosine term in Eq. (1) in weak fields $\omega_c\tau \ll 1$ is much less transparent. In this limit, we have $\sigma_{xy} = \sigma_0\omega_c\tau$ in the argument of cosine. The cosine term can be also rewritten as

$$\cos[2\pi(k_F l)(\omega_c\tau)] = \cos\left(\frac{2\pi l^2}{l_B^2}\right) = \cos\left(\frac{2\pi B l^2}{\Phi_0}\right), \quad (6)$$

where l_B is the magnetic length and Φ_0 is the flux quantum. For comparison, in the strong-field limit, the cosine term can be cast in the form

$$\cos\left(2\pi B R_L^2/\Phi_0\right). \quad (7)$$

Comparing this expression to the last cosine in Eq. (6) suggests that, in weak fields, the role of the Larmour radius is taken by the mean-free path l. Note that l does not depend on magnetic field. Then, the following question arises: What physics causes the orbital action of the magnetic field to manifest itself in the scaling equations in the weak-field limit? A possible way to unveil the orbital action is to adopt a cartoon picture where an electron moves not in a random potential but rather in a *periodic* background, say, on a quadratic lattice, as in seminal paper Ref. 30. Then, we have to assume that the lattice constant l is *set by disorder*. In this cartoon, the orbital action will be encoded into the structure of the Bloch wave functions of electrons. It is the structure of the Bloch wave functions that leads to edge states in the presence of boundaries.[30] Note that the structure of the Bloch wave functions in a magnetic field depends crucially on the number of flux quanta through the unit cell, which, upon identifying l with the lattice constant, is the argument of the cosine in Eq. (6). Then, the factor $\exp[-2\pi k_F l]$ in front of the cosine in Eq. (1) has a meaning of degree to which a realistic random potential can be viewed as a periodic. Indeed, this factor can be interpreted as a probability for a realistic diffusive electron to execute the *same* loop of length $\sim l$ more than once.

Obviously, a realistic disordered system does not have any built-in spatial periodic structure. In view of the lack of a transparent interpretation of topological term in the weak-magnetic-field limit, it is important to check numerically whether or not some discrete value of the magnetic field of the order of $B \sim \Phi_0/l^2$ causes delocalization transition and formation of edge state in a random potential. This was a subject of the papers in Ref. 31. In these papers, a network model describing a weakly chiral electron motion was introduced. The position of the quantum delocalization transition was established from the conventional transfer-matrix simulation of the transmission of the network. It was demonstrated that up to $k_F l \sim 10$, the above estimate for the transition field applies. However, quantum simulations become progressively complex in the limit of vanishing field.

B. Delocalization transition with strong spatial inhomogeneity

In this paper, we establish the position of delocalization transition indirectly. The underlying idea of our approach is that, when a strong spatial inhomogeneity is introduced into the quantum network, interference effects become progressively irrelevant in the sense that *amplitudes* of each two interfering paths typically differ strongly. Then, the problem of the transport through a network reduces to the *classical percolation*. Most importantly, while the inhomogeneity-induced suppression of quantum interference leads to a strong reduction of the localization radius, the *position* of the transition remains unchanged. At the same time, classical simulations can be extended to a much weaker magnetic field. The main outcome of our simulations is that, for very weak fields (very small $\omega_c\tau$) or high electron energies (very large $k_F l$), the transition field is higher than Φ_0/l^2, namely,

$$B \sim \frac{\Phi_0}{l^2}(k_F l)^\kappa, \quad (8)$$

where κ is close to 1/2. In terms of the flow diagram of the quantum Hall effect,[3] the result Eq. (8) translates into the prediction that, for $\sigma_{xx} > 10$, the vertical flow line in Fig. 1(b) deviates from $\sigma_{xy} = 1/2$ to the right.

In this paper, we also study levitation of delocalized states in a vanishing *average* magnetic field, but in the presence of a strongly fluctuating *random* magnetic field. There is a notion that electron density variations near the half-filling $\nu = 1/2$ of the lowest Landau level reduces to a random magnetic field acting on composite fermions.[32,33] It is also possible to realize an inhomogeneous magnetic field, acting on 2D electrons, artificially.[34–42] Different aspects of electron motion in random magnetic fields have been studied theoretically in Refs. 43–56.

Fractional quantum Hall transitions can be associated with quantization of cyclotron orbits of composite fermions. In this sense, fractional quantum Hall transitions are the counterparts of delocalization transitions of electrons. Then, the question arises as to whether a delocalization transition for electrons at vanishing magnetic fields has its counterpart for composite fermions at vanishing $|\nu - 1/2|$. At such filling factors, composite fermion "feels" very weak average magnetic field. On the other hand, local fluctuations of electron density give rise to a very strong *random* magnetic field, acting on composite fermion. For this situation, we reduce the description of magnetotransport to a different percolation problem. For critical values of filling factors, we obtain $|\nu - 1/2| \sim (k_F l)^{-0.4}$.

II. WEAKLY CHIRAL NETWORK MODEL

A. Description

For completeness, we remind the construction of the network model introduced in Refs. 31 to describe quantum electron motion in a weak magnetic field. This construction is illustrated in Fig. 2 and consists of three steps.

(i) We restrict electron motion by introducing forbidden regions A_{nm} (gray areas in Fig. 2), which are not accessible for electrons. Then, the electron moves in both directions along the links, which are the white regions, separating A_{nm}. The links join each other at the nodes, shown in Fig. 2 with brown full circles.

(ii) We forbid forward and backward scattering at the nodes. This allows us to parametrize the node scattering matrix S_q by a single parameter q as follows:

$$\begin{pmatrix} Z_2 \\ Z_4 \\ Z_6 \\ Z_8 \end{pmatrix} = \begin{pmatrix} 0 & -\sqrt{1-q} & 0 & -\sqrt{q} \\ \sqrt{q} & 0 & \sqrt{1-q} & 0 \\ 0 & -\sqrt{q} & 0 & \sqrt{1-q} \\ \sqrt{1-q} & 0 & -\sqrt{q} & 0 \end{pmatrix} \begin{pmatrix} Z_1 \\ Z_3 \\ Z_5 \\ Z_7 \end{pmatrix}, \qquad (9)$$

where Z_i are the amplitudes of incoming and outgoing waves (see Fig. 2).

(iii) We incorporate backscattering of an electron moving along the link. The probability of backscattering is p, so that the corresponding scattering matrix S_p has the form

$$\begin{pmatrix} Z_1 \\ \tilde{Z}_2 \end{pmatrix} = \begin{pmatrix} \sqrt{1-p} & \sqrt{p} \\ -\sqrt{p} & \sqrt{1-p} \end{pmatrix} \begin{pmatrix} \tilde{Z}_1 \\ Z_2 \end{pmatrix}, \qquad (10)$$

where $\tilde{Z}_1$ and Z_2 are amplitudes of incident waves, whereas Z_1 and $\tilde{Z}_2$ are amplitudes of reflected waves (see Fig. 2).

B. Relation to observables: Parameter *p*

To establish a correspondence with physical parameters, we identify the lattice constant with the mean-free path l. Note that, even at $p = 0$ (without backscattering), the classical electron would execute a diffusive motion over the network Fig. 2 due to scattering at nodes. However, a specific aspect of the diffusive motion with $p = 0$ is that it *does not* allow quantum weak localization corrections. Indeed, weak localization corrections originate from the trajectories on the network for which an electron, starting from a certain link, returns to the same link with *opposite* direction of velocity (coherent backscattering). At $p = 0$, the electron still can return to the same link, e.g., by encircling one forbidden region, but its velocity will be *the same* as the initial velocity. Finite p gives rise to weak localization. An example of an elementary loop providing coherent backscattering is shown in Fig. 2. The probability of this loop is

$$\mathcal{P} = p(1-p)^4[q(1-q)]^3. \qquad (11)$$

On the other hand, for a realistic electron, the return probability is $(k_F l)^{-1}$. This allows us to identify the parameter p as

$$p = \frac{1}{k_F l} = \frac{1}{\sigma_0}. \qquad (12)$$

We emphasize that $\sigma_0 = 1/p$ is the Drude conductivity at scales of the order of the mean-free path. This should not be confused with conductance of the sample σ_{xx}, which is the power transmission coefficient through the *entire* network. While the latter can not exceed 1, σ_0 can be arbitrarily big.

Additional justification for identifying Drude conductivity with $1/p$ comes from zero-field scaling theory of localization.[1] According to this theory, localization radius ξ depends on Drude conductivity as $\ln \xi = \pi\sigma_0/2$ with time-reversal symmetry, and $\ln \xi = \pi^2\sigma_0^2$ without time-reversal symmetry. On the other hand, in Ref. 31, the dependence $\ln \xi$ versus p at $q = 1/2$ has been studied for our model by means of quantum simulations. The results presented in Fig. 15 of Ref. 31 are in agreement with scaling theory predictions if p is identified with $1/\sigma_0$.

C. Relation to observables: Parameter *q*

We will relate the parameter q to magnetic field in two ways: quantum mechanically and classically. Quantum mechanically, following Refs. 57–59, one can express the Hall resistance of the node R_H via the elements of matrix S_q [Eq. (9)]:

$$R_H = \frac{2q-1}{q^2 + (1-q)^2}. \qquad (13)$$

In the absence of magnetic field, R_H vanishes, indicating that $(1/2 - q)$ is a measure of magnetic field, which is also the degree of preferential scattering to the left over scattering to the right. For a realistic electron moving a distance l in a magnetic field, this degree is $\omega_c\tau$, thus allowing the following identification:

$$\tfrac{1}{2} - q = \omega_c\tau. \qquad (14)$$

Classical derivation of Eq. (14) emerges from the following reasoning. The presence of two types of scattering processes, on the links and at the nodes, makes the Boltzmann description of transport more complex. To develop this description, we turn to Fig. 3. It illustrates that the adequate variables to describe the Boltzmann transport are the probabilities, ρ_i, $i = 1, \ldots, 8$, to

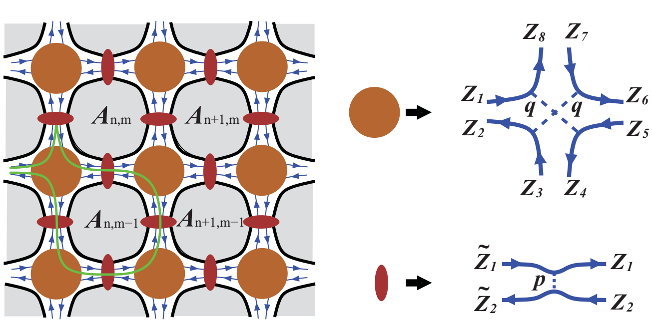

FIG. 2. (Color online) Left: Restricted electron motion over point contacts and bend junctions is illustrated; $A_{n,m}$ are the centers of forbidden regions. Green (gray) line shows a minimal loop that can be traversed in clockwise and anticlockwise directions. Right: Scattering matrices at the node and at the link.

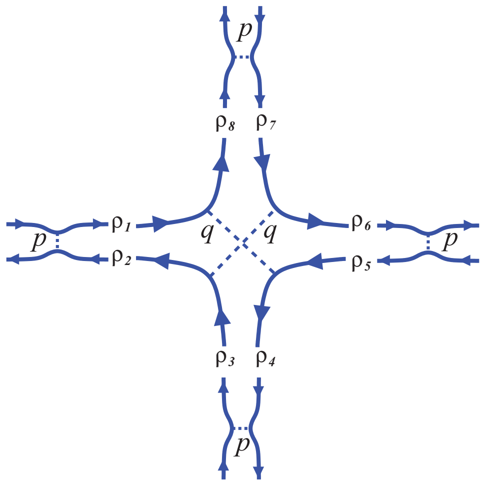

FIG. 3. (Color online) Boltzmann transport on the p-q network. Rate equations (15) relate the probabilities $\rho_i(m,n;t)$ to find an electron on the corresponding half-link adjacent to the node with coordinates (m,n) and at time instances t and $t+\tau$.

find an electron on corresponding half-link. In these variables, the closed set of rate equations reads as

$$\begin{aligned}
\rho_1(m,n;t+\tau) &= [1-p]\rho_6(m-1,n;t) + p\rho_2(m,n;t),\\
\rho_2(m,n;t+\tau) &= [1-q]\rho_3(m,n;t) + q\rho_7(m,n;t),\\
\rho_3(m,n;t+\tau) &= [1-p]\rho_8(m,n-1;t) + p\rho_4(m,n;t),\\
\rho_4(m,n;t+\tau) &= [1-q]\rho_5(m,n;t) + q\rho_1(m,n;t),\\
\rho_5(m,n;t+\tau) &= [1-p]\rho_2(m+1,n;t) + p\rho_6(m,n;t),\\
\rho_6(m,n;t+\tau) &= [1-q]\rho_7(m,n;t) + q\rho_3(m,n;t),\\
\rho_7(m,n;t+\tau) &= [1-p]\rho_4(m,n+1;t) + p\rho_8(m,n;t),\\
\rho_8(m,n;t+\tau) &= [1-q]\rho_1(m,n;t) + q\rho_5(m,n;t). \qquad (15)
\end{aligned}$$

Performing Fourier transform in time and coordinate domains and taking the limit of small momenta k and frequencies ω_k, we find a diffusive mode $-i\omega_k = Dk^2$, where D is given by

$$D = \left(\frac{l^2}{4\tau}\right)\frac{1-p}{8}\,\frac{1+(2q-1)^2(2p-1)}{1+(2q-1)^2(2p-1)^2}. \qquad (16)$$

As discussed above, the diffusion coefficient is finite even at $p=0$, except in the "strong-field" limits $q=1$ and $q=0$, where the electron circulates around forbidden regions clockwise and anticlockwise, respectively. In these limits, for small p, the diffusion coefficient is proportional to p. From Eq. (17), we also see that $D \to 0$ in the strong-scattering limit $p \to 1$, as could be expected. In the limit of weak magnetic field $(1/2-q) \ll 1$ and high mobility $p \ll 1$, we have

$$D = \left(\frac{l^2}{32\tau}\right)\left[1-p-8\left(\frac{1}{2}-q\right)^2\right]. \qquad (17)$$

The fact that the magnetic-field correction to D is $\sim(\omega_c\tau)^2$ is generic for classical magnetotransport. On the other hand, the negative classical correction to D due to finite p is model specific, since p was incorporated to capture interference effects. The meaning of the prefactor l^2/τ, which emerges from the system Eq. (15) in the course of Fourier transform, is that the electron travels the distance of the mean-free path l during scattering time τ. Correct, within a number, prefactor and magnetic-field dependencies of D indicate that the network model captures properly the magnetotransport in high-mobility electron gas in the Boltzmann limit.

To conclude the construction of the quantum network, we assume as usual that random phases are accumulated in the course of propagation along the links. This convention is nontrivial in the weak-field limit. Indeed, as we discussed in the Introduction, the delocalization transition is expected when the magnetic flux through a plaquette is of the order of flux quantum Φ_0. We will return to this point in Sec. IV D.

According to the scaling theory of localization, the knowledge of the Boltzmann transport coefficient should be sufficient to predict the position [Eq. (4)] of the *quantum* delocalization transitions, which in the limit of weak fields takes the form $E_0 \sim \hbar/\omega_c\tau^2$. In the language of the network model, this translates into the linear dependence

$$p \sim \tfrac{1}{2} - q. \qquad (18)$$

Whether or not this prediction is valid can be established only by quantum numerical simulations. Especially important is the limit $q \to 1/2$, which corresponds to vanishing magnetic fields where a strong levitation is expected. Unfortunately, this limit is the hardest to simulate. This is because the localization radius to the left and to the right of the delocalization transition is huge, i.e., $\ln(\xi/l) = \pi^2\sigma_0^2 \sim \pi^2/p^2$. This was a limitation of the quantum simulations reported in Ref. 31, where the smallest value of p was $p = 0.1$.

D. From quantum delocalization to classical percolation

There is another, indirect, way to find the critical p-q boundary, bypassing quantum simulations, namely, to take the limit of strong disorder. By a limit of strong disorder, we mean that *local* values p_i and q_i are strongly spread around averages p and q with distributions

$$f(p_i) = p\,\delta(1-p_i) + (1-p)\delta(p_i), \qquad (19)$$
$$f(q_j) = q\,\delta(1-q_j) + (1-q)\delta(q_j). \qquad (20)$$

Unlike the quantum case, where p_i and q_i were the same for all links and nodes, with distribution, Eq. (19) scatterers on the links reflect *fully* in p percent of the cases and transmit fully in the rest in $(1-p)$ percent of cases. Similarly, according to Eq. (20), the nodes deflect only to the right in q^2 percent of the cases, deflect only to the left in $(1-q)^2$ percent of the cases; in the remaining $2q(1-q)$ percent of the cases, the deflection takes place both to the left and to the right depending on the incoming channel (see Fig. 4). The advantage of the strong-disorder limit is that the quantum interference effects are irrelevant. The simplest way to see this is to turn to the elementary interference process illustrated in Fig. 2. If return to the origin is allowed for the clockwise direction, then it is forbidden for the anticlockwise direction since $q_i(1-q_i)$ is zero in the strong-disorder limit.

In the absence of interference, the transport reduces to the classical bond percolation problem. The reduction is

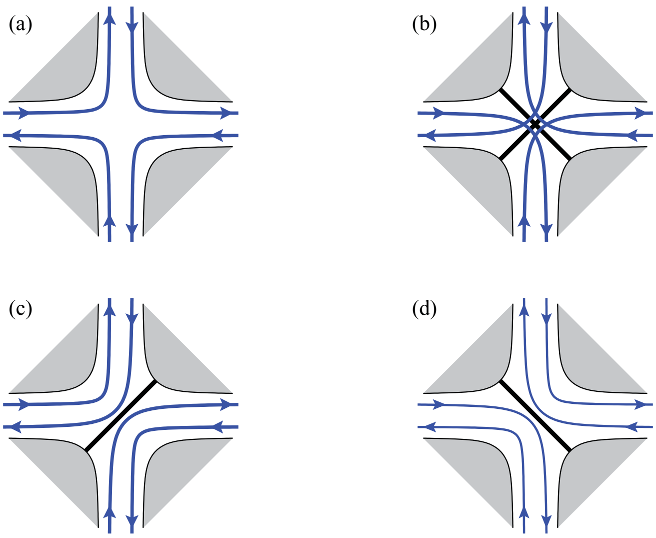

FIG. 4. (Color online) Definition of the q bonds. Scattering scenarios (a), (b), (c), and (d) correspond to the absence of both q bonds, presence of both q bonds, presence of one right-diagonal q bond, and presence of one left-diagonal q bond, respectively.

achieved by replacing scattering matrices (9) and (10) by bonds according to the following rules:

(i) The realization in which $p_i = 1$ corresponds to quantum mechanical reflection of incoming waves from all directions. In the language of percolation, this configuration corresponds to a *bond* installed between the neighboring forbidden regions $A_{n,m}$ and $A_{n+1,m}$, i.e., the horizontal bond in Fig. 2. Below, we refer to this bond as a p bond. For configurations with $p_i = 0$, the p bond between the neighboring forbidden regions $A_{n,m}$ and $A_{n+1,m}$ is absent.

(ii) The scattering matrix S_q is replaced by a *pair* of bonds (we refer to them as q bonds), installed between the forbidden regions $A_{n,m}$ and $A_{n\pm1,m\pm1}$, i.e., diagonal bonds in Fig. 2. Both q bonds are absent [Fig. 4(a)] if the node deflects only to the left. Probability of this realization is $P_a = (1-q)^2$, as follows from Eq. (20). Deflection only to the right corresponds to two crossed q bonds present [Fig. 4(b)]. This happens with probability $P_b = q^2$. The situation when right-diagonal q bond is present while the left-diagonal q bond is absent corresponds to the scattering scenario in Fig. 4(c). The opposite scattering scenario [Fig. 4(d)] translates into left-diagonal q bond present and right-diagonal q bond absent. The two latter bond configurations have equal probabilities $P_c = P_d = q(1-q)$.

Quantum mechanical delocalization transition in the limit of strong disorder corresponds to percolation over p and q bonds (see Fig. 5). At the threshold of percolation, p and q bonds form an infinite cluster. At the same point, the waves propagating along the links in both directions and scattered at the links and at the nodes form an edge state. Threshold (q,p) values lie on a critical line of transitions on a q-p plane. Crucial for us is the relation between the points of this line and the positions of quantum delocalization transitions. In this regard, it is important to relate the quantum matrix S_q to the matrices describing the different classical scenarios shown in

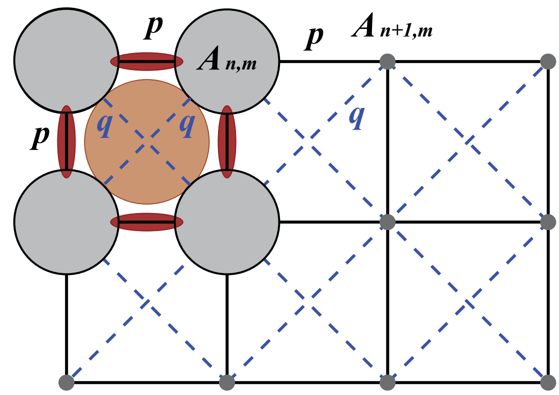

FIG. 5. (Color online) Limit of strong disorder. The centers of forbidden regions $A_{n,m}$ and $A_{n,m-1}$ are connected by the p bond, while the centers of forbidden regions $A_{n-1,m-1}$ and $A_{n,m}$ are connected by a q bond. The delocalization transition corresponds to the percolation threshold on the lattice consisting of p and q bonds.

Fig. 4. Setting $q = 0$, we get

$$S_a = \begin{pmatrix} 0 & -1 & 0 & 0 \\ 0 & 0 & 1 & 0 \\ 0 & 0 & 0 & 1 \\ 1 & 0 & 0 & 0 \end{pmatrix}, \tag{21}$$

which describes the scattering in Fig. 4(a). The scattering scenario in Fig. 4(b) is described by the matrix

$$S_b = \begin{pmatrix} 0 & 0 & 0 & -1 \\ 1 & 0 & 0 & 0 \\ 0 & -1 & 0 & 0 \\ 0 & 0 & -1 & 0 \end{pmatrix}, \tag{22}$$

which emerges upon setting $q = 1$ in Eq. (9). To get the matrix

$$S_c = \begin{pmatrix} 0 & 0 & 0 & -1 \\ 0 & 0 & 1 & 0 \\ 0 & -1 & 0 & 0 \\ 1 & 0 & 0 & 0 \end{pmatrix}, \tag{23}$$

one has to set $q = 0$ in the first and third columns, and $q = 1$ in the second and fourth columns. Similarly, the matrix

$$S_d = \begin{pmatrix} 0 & -1 & 0 & 0 \\ 1 & 0 & 0 & 0 \\ 0 & 0 & 0 & 1 \\ 0 & 0 & -1 & 0 \end{pmatrix}, \tag{24}$$

corresponding to Fig. 4(d), emerges upon setting $q = 1$ in the first and third columns and $q = 0$ in the second and fourth columns.

Matrices S_a and S_b provide nonzero Hall resistances $R_H^a = -1$, $R_H^b = 1$, while for S_c and S_d, we have $R_H^c = R_H^d = 0$, i.e., the Hall resistances are zero. The net Hall resistance is thus determined by

$$P_a R_H^a + P_b R_H^b = P_b - P_a, \tag{25}$$

which should be proportional to the magnetic field $(1/2 - q)$. The other relations between the probabilities of different scattering scenarios are normalization $P_a + P_b + P_c + P_d = 1$, and obvious symmetry $P_c = P_d$. These relations do not fix all probabilities uniquely. There is a profound physical reason for this ambiguity. Indeed, the net Hall resistance can be zero even if nodes locally deflect either to the left or to the right provided that $P_a = P_b$. This corresponds to the situation when a random magnetic field with zero average acts on electron, so that the time-reversal symmetry is broken even in the absence of an external field. Such a situation is generic for composite fermions, as was discussed in the Introduction.

In addition to the probability assignment

$$P_a = (1-q)^2, \quad P_b = q^2, \quad P_c = P_d = q(1-q), \tag{26}$$

dictated by Eq. (20) and described above, one can choose, e.g.,

$$P_a = 1-q, \quad P_b = q, \quad P_c = P_d = 0, \tag{27}$$

when the electron scatters only to the left or only to the right from all incident channels. Obviously, for the latter assignment, the magnitude of the random magnetic field is stronger than for assignment Eq. (26). Finally, the physical situation when the time-reversal symmetry is preserved in zero external magnetic field corresponds to

$$P_a = 1-2q, \quad P_b = 0, \quad P_c = P_d = q. \tag{28}$$

Three variants Eqs. (26)–(28) define three different percolation models, which we denote as $\mathcal{A}$, $\mathcal{B}$, and $\mathcal{C}$, respectively. Results of numerical simulations of these models are reported in the next section.

In conclusion of this section, we would like to draw a contrast between the classical limits of 4×4 scattering matrix S_q and of 2×2 scattering matrix S_p [Eq. (10)]. Unlike the scattering matrix S_q, there is no ambiguity in taking the strong-disorder limit of the 2×2 link matrix S_p because this limit corresponds to the presence or absence of a *single* bond. In this regard, note that, in a fully chiral network model by Chalker and Coddington,[60] scattering at the nodes is also described by a 2×2 scattering matrix. The limit of strong disorder corresponds to the presence or absence of a single bond between the centers of the squares $A_{n,m}$. Taking a strong-disorder limit in the Chalker-Coddington model reduces the quantum problem to conventional bond percolation on a square lattice. The position of the percolation threshold and the quantum delocalization transition certainly coincide, while the localization length in the strong-disorder limit is smaller.[61]

III. SIMULATION PROCEDURE AND RESULTS

In simulations performed, disorder realizations correspond to the presence or absence of p and q bonds. In each realization, probabilities of p and q bonds are specified by the rules formulated above. Convention for the p bonds, connecting counterpropagating links of $n+m$ odd and $n+m$ even sublattices is the same for all three models. Conventions for q bonds are different for the models $\mathcal{A}$, $\mathcal{B}$, and $\mathcal{C}$. These conventions are specified by Eqs. (26)–(28), respectively. The main peculiarity of the simulations that complicates the trajectories stems from arrangement of pairs of q bonds at the nodes. Namely, for different directions of approach to the given node, the outcomes of passage are *correlated*. These correlations are illustrated in Fig. 5. The models $\mathcal{A}$, $\mathcal{B}$, and $\mathcal{C}$ differ by the weights with which different outcomes a, b, c, or d (Fig. 5) are allowed.

The size L of the samples used ranged between 500 and 10 000, where our unit of distance is half a link. For the largest system, we average over 10^6 disorder realizations. This number increases with decreasing size so that we keep a roughly constant CPU effort per size. To locate the position of the percolation threshold, we searched for trajectories connecting two opposite faces of a square sample (periodic boundary conditions were imposed in the perpendicular direction). As in Ref. 62, for a given realization, the two-terminal conductance between the opposite open faces was identified with the number of such spanning trajectories. Different disorder realizations generate the conductivity distribution with average $\sigma(q,p,L)$.

A. Phase diagrams

To determine the critical boundary for each of the three models considered, $p_{\mathcal{A}}(q)$, $p_{\mathcal{B}}(q)$, and $p_{\mathcal{C}}(q)$, we select a set of values of the turning probability q and then scan for many values of the probability p. For each size L, we represent the conductance as a function of p on a logarithmic scale and fit the points near the maximum of the conductance by a Gaussian. We then plot the position of the peak as a function of L^{-1} and extrapolate to infinite size. We found empirically that this fitting procedure is of high quality for the three models.

In Fig. 6, we represent the critical lines obtained for the three models: the upper curve corresponds to model $\mathcal{B}$, the curve in the middle to model $\mathcal{A}$, and the lower curve to model $\mathcal{C}$. The straight line corresponds to $p = 1/2 - q$. The solid dots are the results of the quantum simulations in Ref. 31. The inset shows the same critical lines as in the main panel at larger scale near the point (1/2,0).

We note that the curves tend to the point (1/2,0) as a power law with power *higher than linear*. To gain further insight,

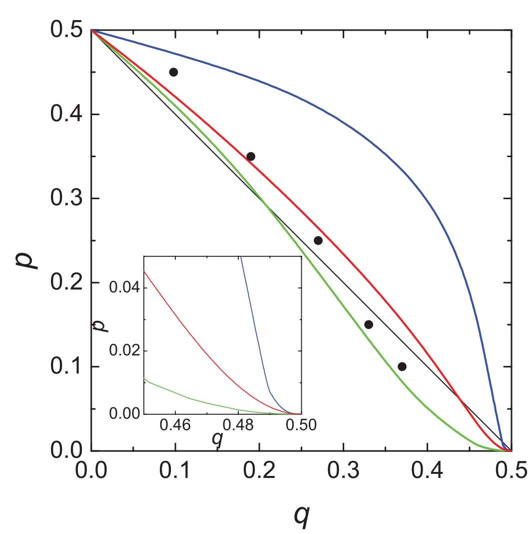

FIG. 6. (Color online) Critical lines for the three models considered: $\mathcal{A}$ (red, middle curve), $\mathcal{B}$ (blue, upper curve), and $\mathcal{C}$ (green, lower curve). The dots are the results of quantum simulations (Ref. 31). Inset shows the same three critical curves at at higher scale near the point (1/2,0).

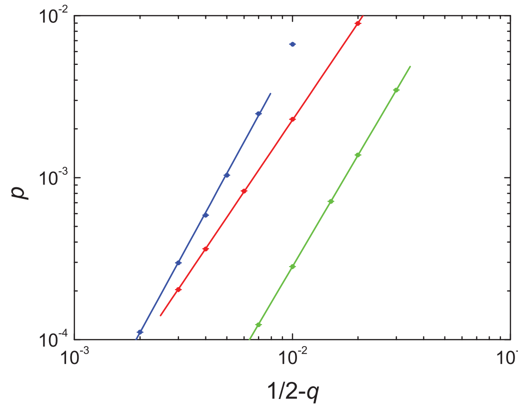

FIG. 7. (Color online) Critical lines for the three models considered: $\mathcal{A}$ (red, middle curve), $\mathcal{B}$ (blue, upper curve), and $\mathcal{C}$ (green, lower curve) on a double logarithmic scale near the point (1/2,0).

we analyze in detail the shape of the phase boundary at small probabilities p. In this regime, q_c is close to 1/2 and we expect a relation of the form

$$p \propto \left|q - \tfrac{1}{2}\right|^{\gamma}. \tag{29}$$

In Fig. 7, we show p versus $q - 1/2$ on a double logarithmic scale for the three models $\mathcal{A}$ (middle set of points), $\mathcal{B}$ (upper set), and $\mathcal{C}$ (lower set). The straight lines are linear fits to the corresponding points. Their slopes are $\gamma_{\mathcal{A}} = 1.994 \pm 0.001$, $\gamma_{\mathcal{B}} = 2.464 \pm 0.001$, and $\gamma_{\mathcal{C}} = 2.286 \pm 0.001$. The errors quoted are the statistical errors; systematic errors are also present since it is impossible to include all finite-size effects.

B. Conventional percolation behavior away from $q = 1/2$

Quantum simulations in Ref. 31 demonstrated that the delocalization transition along the boundary $p(q)$ belongs to the quantum Hall universality class. In particular, it was demonstrated that, for the first three black dots in Fig. 6, which correspond to $q < 0.3$, the critical exponent is close to 7/3. Introducing strong disorder suppresses the quantum interference. We expect that quantum percolation at a given (q,p) reduces to classical percolation and the critical exponent $\nu = 7/3$ is replaced by its classical value $\nu = 4/3$. For the Chalker-Coddington model, in which the position of delocalization is fixed at average value of the disorder potential, the crossover from 7/3 to 4/3 was tested in Ref. 61. In this section, we demonstrate that, *away from the point* $p = 0, q = 1/2$, the $p(q)$ boundary established above indeed corresponds to the divergence of the localization length with exponent $\nu = 4/3$.

The determination of the critical exponent is based on the fact that near $(q,p) = (q_c,p_c)$, the conductance is a function of a single argument $(p - p_c)L^{1/\nu}$ (vertical scan) or $(q - q_c)L^{1/\nu}$ (horizontal scan). Exactly at (q_c,p_c), the conductivity assumes the universal value $\sigma_0 = 0.361\,404\ldots$ found by Cardy,[63] which should be the same for the entire boundary.

The scaling analysis was performed for all three models. In Fig. 8, we present results for the model $\mathcal{A}$ at a particular critical point (0.3,0.23392). Overall, the scaling confirms that $\nu = 4/3$ both for vertical and horizontal scans. A particular feature about the scaling data is that the widths of scaling functions are slightly different for the vertical and horizontal scans. We

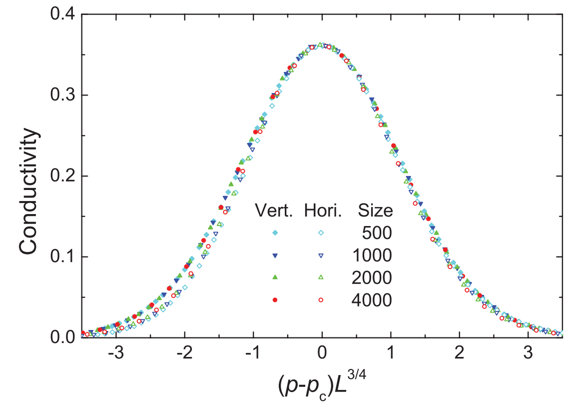

FIG. 8. (Color online) Scaled conductivity as a function of the probability difference with the critical point multiplied by $L^{3/4}$. The solid symbols correspond to vertical scans and the empty symbols to horizontal scans crossing the critical point (0.3,0.23392) of model $\mathcal{A}$. The lateral sample sizes are 500 (cyan diamonds), 1000 (blue down triangles), 2000 (green up triangles), and 4000 (red circles).

have also found that there is a small size effect precisely at the boundary, which is well described by the expression

$$\sigma_L = \sigma_0 + \frac{a}{L^{3/4}}, \tag{30}$$

where a is a constant.

C. Behavior of the localization length at zero field: Models $\mathcal{A}$ and $\mathcal{C}$.

We now turn to the behavior of the localization length ξ at zero magnetic field $q = 1/2$. For each model, the dependence $\xi(p)$ at small p is determined by a peculiar behavior of the corresponding delocalization boundary established in Sec. III A. It is also very important that $\xi(p)$ is equally affected by the second, complementary, boundary in the domain $q > 1/2$, which is the mirror image of the boundary in Fig. 6.

For moderate p, when the boundaries were straight lines,[31] the presence of the second boundary leads to the enhancement of ξ. On the contrary, we will see that, in the limit $p \to 0$, the fact that both boundaries for a given model are almost horizontal leads to a shortening of ξ.

In Fig. 9, we plot the conductivity for model $\mathcal{A}$ as a function of p for $q = 1/2$ and for several values of the system size: 500 (diamonds), 1000 (down triangles), 2000 (up triangles), 4000 (circles), and 8000 (squares). It is seen that the curves $\sigma(p)$ for different system sizes have similar shapes and are even spaced along the logarithmic horizontal axis. Thus, we expect scaling and behavior $\xi \sim p^{-\nu_{\mathcal{A}}}$ as a consequence. A practical procedure to infer $\nu_{\mathcal{A}}$ from the data in Fig. 9 is based on the dependence p_L versus L, where p_L is the position of the maximum of the conductivity for a given L. In the inset of Fig. 9, we plot $p_L(L)$ in a double logarithmic scale. We see that p_L follows the dependence

$$p_L = bL^{-\beta}, \tag{31}$$

where b and β are model-dependent constants. For model $\mathcal{A}$, we found $\beta_{\mathcal{A}} = 1.51 \pm 0.02$ and $b = 4.1 \pm 0.8$. Equation (31) and the fact that $\beta_{\mathcal{A}}$ is very close to 3/2 suggest that, to achieve

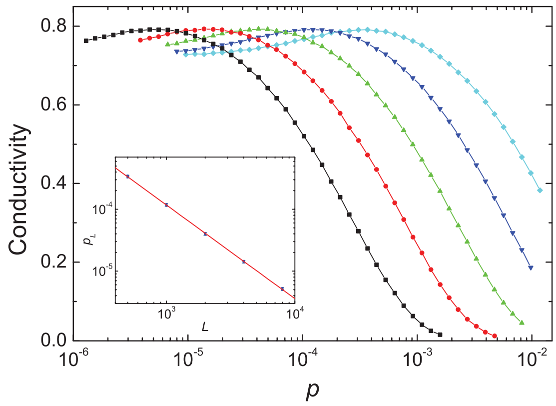

FIG. 9. (Color online) Conductivity as a function of p for model $\mathcal{A}$ along the line $q = 1/2$. The lateral sample sizes are 500 (cyan diamonds), 1000 (blue down triangles), 2000 (green up triangles), 4000 (red circles), and 8000 (black squares). Inset shows the position of the peaks as a function of L on a double logarithmic scale.

scaling, the data in Fig. 9 should be replotted versus $pL^{3/2}$. The result of this replotting is shown in Fig. 10. It is seen that the overlap is excellent, yielding the critical exponent $\nu_{\mathcal{A}} = 2/3$. This should be contrasted to the behavior $\xi(p) \propto (p - p_c)^{-4/3}$ at *any* nonzero p_c. We conclude that, at $p_c = 0$, the divergence of the localization length with p is much slower.

Finally, for the model $\mathcal{C}$, the plots $\sigma(p)$ as a function of p do not exhibit maxima. As shown in Fig. 11, where we plot $\sigma(p)$ versus $pL^{7/4}$, a very good overlap is achieved for $\nu_{\mathcal{C}} = 4/7$.

In conclusion of this section, we note that the conductivity for all three models tends to $2\sigma_0 = 0.722\,808\ldots$ as $p \to 0$. The reason is that the value $\sigma = \sigma_0$ at the threshold is the property of a *single* critical point.[63] By contrast, in our case, *two* critical lines merge at the point $q = 1/2$, $p = 0$.

D. Behavior of the localization length at zero field: Model $\mathcal{B}$

Scaling analysis of the data for model $\mathcal{B}$ reveals slightly different behaviors for the domains of moderate $p > 10^{-4}$ and truly critical $p < 10^{-4}$. For the first domain, from the position of peaks, we find $\beta_{\mathcal{B}} = 1.77 \pm 0.04$. This suggests that $\nu_{\mathcal{B}} = 1/\beta_{\mathcal{B}} \approx 4/7$. Note, however, that replotting the conductivity

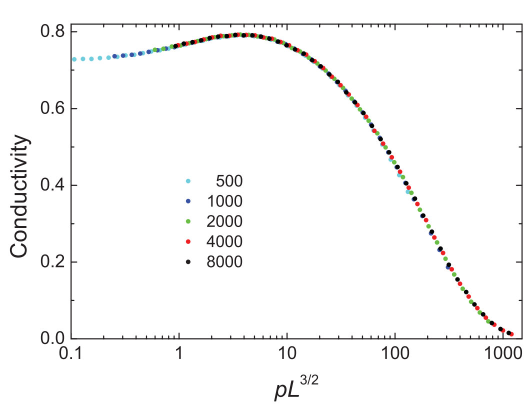

FIG. 10. (Color online) Conductivity as a function of $pL^{3/2}$ on a logarithmic scale for model $\mathcal{A}$ along the line $q = 1/2$. The sample sizes are 500 (cyan), 1000 (blue), 2000 (green), 4000 (red), and 8000 (black).

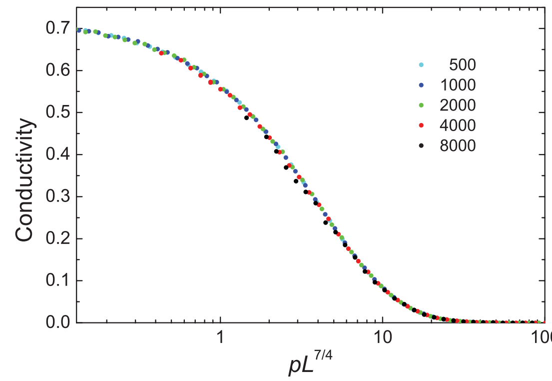

FIG. 11. (Color online) Conductivity as a function of $pL^{7/4}$ on a logarithmic scale for model $\mathcal{C}$ along the line $q = 1/2$. The sample sizes are 500 (cyan), 1000 (blue), 2000 (green), 4000 (red), and 8000 (black).

versus $pL^{7/4}$ (see Fig. 12) does not lead to overlap as good as for the model $\mathcal{A}$. Moreover, in the second domain $p < 10^{-4}$, a good overlap is achieved for the exponent 2/3, i.e., the same as in the model $\mathcal{A}$. This is illustrated in the inset of Fig. 12. This indicates that, for the model $\mathcal{B}$, the true critical region is quite narrow. Such a delicate behavior of $\xi(p)$ for the model $\mathcal{B}$ might indicate that the critical boundary $p(q)$ in this model also changes the behavior in the truly critical region $p \lesssim 10^{-4}$.

IV. DISCUSSION

A. Position of boundaries

It is seen from Fig. 6 that the boundaries $p_{\mathcal{A}}(q)$ and $p_{\mathcal{C}}(q)$ almost coincide in the entire domain $0 < q < 1/2$. Overall, these boundaries are in agreement with the results of quantum simulation Ref. 31 shown with black dots. It is also seen that the boundary $p_{\mathcal{B}}(q)$ goes significantly higher. In particular, at $q = 0.25$, $p_{\mathcal{B}}$ exceeds $p_{\mathcal{C}}$ almost twice. On the physical level, this means that, for a given average magnetic field, the formation of edge states requires a longer zero-field mean-free path l for model $\mathcal{C}$ than for model $\mathcal{B}$. In other words, formation

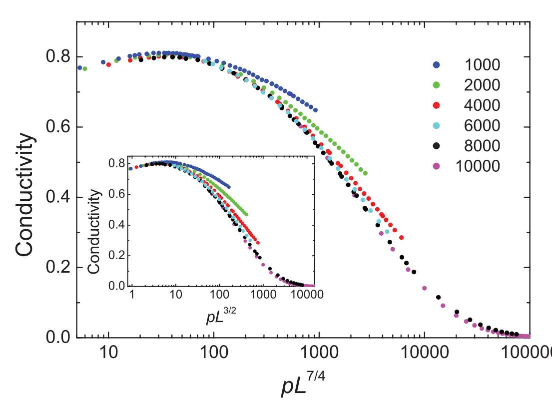

FIG. 12. (Color online) Conductivity as a function of $pL^{7/4}$ along the line $q = 1/2$ on a logarithmic scale for model $\mathcal{B}$. The sample sizes are 1000 (blue), 2000 (green), 4000 (red), 6000 (cyan), 8000 (black), and 10 000 (magenta). Inset: The same as main plot with low-p data included; conductivity is plotted versus $pL^{3/2}$.

of edge states happens easier when a random magnetic field is present. To gain a physical insight as to why this is so, consider electron motion in a random magnetic field. Local value of the field changes its sign in space, while the average field $(1/2 - q)$ is much smaller than the absolute value of the local field. Then, electron trajectories are either circles inside the regions where the field maintains its sign, or snake states, propagating along the boundaries of these regions, i.e., along the contours with zero local field. Then, it is apparent that a weak disorder does not affect this picture. If, on the other hand, the magnetic field $(1/2 - q)$ is uniform, electron trajectories are big circles. Then, a weak disorder will have a strong effect by deflecting an electron before it completes a circle. The above two situations correspond to the models $\mathcal{B}$ and $\mathcal{C}$, respectively, and explain why $p_{\mathcal{B}}(q) > p_{\mathcal{C}}(q)$. In model $\mathcal{A}$, a random component of a magnetic field is present, but is weaker than in model $\mathcal{B}$. In this regard, the fact that the boundary $p_{\mathcal{A}}(q)$ lies between $p_{\mathcal{B}}(q)$ and $p_{\mathcal{C}}(q)$ also finds its explanation.

Five quantum data points of Ref. 31 shown in Fig. 6 cover the range $p \geqslant 0.1$ and follow $p_{\mathcal{C}}(q)$ within the accuracy of quantum simulations. The fact that these points follow the straight line $p = 1/2 - q$ confirms the scaling theory [Eqs. (1) and (2)] for $\sigma_{xx} < 10$. The full confirmation of the scaling theory would be the linearity of the critical percolation boundary at $q \to 1/2$ [see Eq. (18)].

The most important outcome of the present simulation is the inset in Fig. 6. It is seen that at really small $p \sim 0.01$ and q close to 1/2, the behaviors of all three boundaries change dramatically compared to their bodies, namely, they become almost horizontal. All three boundaries have the form $p \sim (1/2 - q)^{\gamma}$ with $\gamma \gtrsim 2$. This is in stark contrast to the prediction of scaling theory [Eq. (18)], which corresponds to $\gamma = 1$. In other words, percolation results suggest that instead of the condition $\sigma_{xy} = 1/2$, the delocalization boundary is described by

$$\sigma_{xy} \sim \sigma_{xx}^{1-\frac{1}{\gamma}}. \tag{32}$$

The latter condition can be also cast in the form Eq. (8) with $\kappa = 1 - 1/\gamma$. We note that the crossover from $\sigma_{xy} = 1/2$ to Eq. (32) takes place at large $\sigma_{xx} \sim 10$. In terms of the flow diagram of the quantum Hall effect,[3] this means that the upper part of the vertical flow line is bent to the right, as it is illustrated in Fig. 1(b).

B. Semianalytical consideration

To specify the distinct behavior of percolation boundaries in vanishing average magnetic field, they are plotted in Fig. 7 in the log-log scale. From the slopes, we deduce the values $\gamma_{\mathcal{A}} = 1.994$, $\gamma_{\mathcal{B}} = 2.464$, and $\gamma_{\mathcal{C}} = 2.286$. To get a feeling why all γ values are close to 2, below we present some semianalytical arguments. We first turn to Fig. 5 and set $p = 0$. Then, the lattice breaks into two quadratic sublattices with $n + m$ even and $n + m$ odd, which are completely disconnected. None of them percolates if q, the percentage of bonds present in each sublattice, is less than 1/2. Finite $p = p_c(q)$ allows percolation for $q < 1/2$ since p bonds couple clusters from different sublattices. It is apparent that coupling of clusters by p bonds is relevant if the typical distance $1/\sqrt{p}$ between two p bonds becomes smaller than the localization length $\xi(q) = (1/2 - q)^{-4/3}$. This yields a constraint that $\gamma < 8/3$. This constraint is insensitive to the mutual correlations of q bonds on the two sublattices. In fact, this correlation is absent in model $\mathcal{A}$. Indeed, as follows from Eq. (26), at $q = 1/2$ for model $\mathcal{A}$, we have $P_a = P_b = P_c = P_d = 1/4$. By contrast, for model $\mathcal{B}$, the probabilities at $q = 1/2$ are $P_a = P_b = 1/2$, $P_c = P_d = 0$. This suggests that q bonds on two sublattices are strongly (and positively) correlated. Namely, if there is a q bond connecting two $n + m$ even plaquettes at a given node, then there must be a q bond connecting $n + m$ odd plaquettes at the same node. On the other hand, the correlation of q bonds at a node in model $\mathcal{C}$ is negative: the presence of one q bond excludes the presence of the other. This is apparent from Fig. 4.

As p bonds are switched on, clusters include sites from both sublattices (see Fig. 13). In Ref. 31 where the model $\mathcal{A}$ was considered, it was argued that $\gamma = 1$. The argument was based on the following picture of the cluster growth upon increasing q: it was assumed that critical q clusters on a given sublattice grow by getting connected via additional q bonds. Since the growth of clusters due to p bonds takes place by connecting critical clusters from different sublattices, it was concluded that p and q bonds play equal roles in the growth of clusters, which immediately leads to $\gamma = 1$. Present simulations suggest that, in the close proximity of $q = 1/2$, this picture fails, and the role of p and q bonds in approaching the percolation threshold is completely different, namely, the growth due to p bonds is more efficient. This growth proceeds by p bonds connecting the *hulls* of critical clusters from two sublattices, as illustrated in Fig. 13. For a given q, the length of the hull is

$$\mathcal{L}(q) = \xi^{7/4}(q) = \left(\tfrac{1}{2} - q\right)^{-7/3}. \tag{33}$$

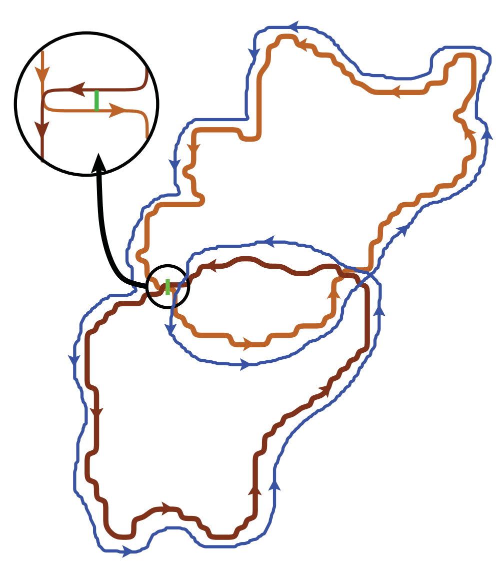

FIG. 13. (Color online) Vicinity of the point $p = 0$, $q = 1/2$ of the phase diagram Fig. 7. A q cluster of $n + m$ odd sublattice (upper) and a q cluster of $n + m$ even sublattice (lower) overlap. A joint trajectory (thin blue line) is formed upon installing of a *single* p bond. The blowup illustrates hybridization of trajectories on a microscopic level.

For the model $\mathcal{A}$, to achieve a percolation by adding p bonds, one should take into account that the hulls on two sublattices are uncorrelated. Then, a p bond with one end on a hull from an even sublattice will have the other end on the hull from an odd sublattice with probability $\mathcal{L}/\xi^2$. As a result, the percolation condition reads as

$$(\mathcal{L}/\xi^2)(p\mathcal{L}) = 1, \tag{34}$$

where the second factor is the probability that there is at least one p bond with one end on the critical hull from, say, the odd sublattice. Equation (34) yields $\gamma_{\mathcal{A}} = 2$, which coincides with the simulation result.

Correlation of q bonds at the nodes for models $\mathcal{B}$ and $\mathcal{C}$ leads to the conclusion that corresponding critical clusters in two sublattices are also correlated. One consequence of this correlation is that it takes less p bonds than in model $\mathcal{A}$ to connect critical hulls from two sublattices. As a result, $\gamma_{\mathcal{B}}$, $\gamma_{\mathcal{C}} \geqslant \gamma_{\mathcal{A}} = 2$. On the other hand, the picture of percolation by connecting the critical clusters imposes the upper boundary $\gamma \leqslant 7/3$ for both models $\mathcal{B}$ and $\mathcal{C}$. This follows from the condition that there should be at least one p bond per critical hull, i.e., $p\mathcal{L} \geqslant 1$. Note that the constraint $\gamma \leqslant 7/3$ is stricter than the constraint $\gamma < 8/3$ established above.

Beyond the estimate $2 \leqslant \gamma_{\mathcal{B}}, \gamma_{\mathcal{C}} \leqslant 7/3$, we can not come up with more accurate analytical values for these indices. We are not even able to establish which of them is bigger. This is because strong correlation between the hulls in both models $\mathcal{B}$ and $\mathcal{C}$ simplifies connectivity upon switching on p bonds. On the other hand, this correlation prevents the expansion of the resulting cluster.

As it was established in the previous section, in the domain of $p \lesssim 10^{-4}$, behavior of $\xi(p)$ at $q = 1/2$ in the model $\mathcal{B}$ exhibits crossover from the critical exponent 4/7 to 2/3. To relate this peculiar behavior with the shape of the percolation boundary $p_{\mathcal{B}}(q) = (1/2 - q)^{\gamma_{\mathcal{B}}}$, we invoke the argument of Ref. 64, which, in application to the p-q model, goes as follows. If the divergence of ξ at the point $q = 1/2$, $p = 0$ is characterized by $\xi \sim (1/2 - q)^{-\nu_q}$ along the q direction and $\xi \sim p^{-\nu_p}$ along the p direction, then the shape of the critical boundary is $p \sim (1/2 - q)^{\nu_q/\nu_p}$, i.e., $\gamma = \nu_q/\nu_p$. Following this argument, crossover in the model $\mathcal{B}$ from $\nu_p = \nu_{\mathcal{B}} = 4/7$ to $\nu_{\mathcal{B}} = 2/3$ suggests that $\gamma_{\mathcal{B}}$ and $\gamma_{\mathcal{A}}$ merge in a truly critical region.

Overall, our numerical results suggest that, in the truly critical domain, where $\gamma_{\mathcal{A}} \approx \gamma_{\mathcal{B}} \approx 2$ and $\gamma_{\mathcal{C}} \approx 7/3$, the divergence of $\xi(p)$ for all three models is well described by the relation

$$\xi \sim p^{-4/(3\gamma)}. \tag{35}$$

With regard to the argument of Ref. 64, this means that, for all three models, the exponent ν_q is equal to 4/3, i.e., the same as for q away from 1/2.

C. Relation to Ref. 62

In Ref. 62, spin quantum Hall effect in bilayer and trilayer systems was studied numerically in order to trace the emergence of macroscopic metallic phase upon adding the third dimension.[65] The authors made use of the fact that, in a strictly 2D system, there is a mapping between the spin quantum Hall transition and classical bond percolation.[66,67] For bilayer systems, the corresponding classical percolation is bond percolation on each layer (bonds connect the centers of plaquettes), complemented with the possibility to switch layers with a probability p_1 while passing each side of each plaquette. Physically, in spin quantum Hall effect, an electron travels on each layer of the network in the same direction. In our consideration of the weak-field quantum Hall effect, an electron stays within a plane, but each link of the square lattice represents two counterpropagating channels. For this reason, there is a mapping between the simulation in Ref. 62 and treatment of the model $\mathcal{A}$ in this paper. Namely, p_1 in Ref. 62 should be identified with the backscattering probability p in this paper, while the probability that the given bond is present in Ref. 62, i.e., p, should be identified with our parameter q. Due to this mapping, critical behavior $p_1(p)$ for small p_1 in Ref. 62 is the same as the behavior of critical line $p \propto (1/2 - q)^{\gamma_{\mathcal{A}}}$ for small p in our model $\mathcal{A}$. Also, the above semianalytical calculation of $\gamma_{\mathcal{A}}$ is the same as proposed in Ref. 62. However, it should be noted that mapping between the network of Ref. 62 and model $\mathcal{A}$ applies only for small p_1. For larger p_1, the position of the boundary in Ref. 62 differs dramatically from that of the model $\mathcal{A}$.

D. Copropagating versus counterpropagating networks

Simulations reported in this paper pertain to the system representing two coupled Chalker-Coddington (CC) networks. Studies of transport in two coupled CC networks were also reported earlier (see Refs. 44,45,62,64,68). For example, in Refs. 44 and 45, two CC networks represented two projections of spin, whereas the coupling represented their mixing due to the spin-orbit interaction. In all previous studies, the result of coupling was the lifting of degeneracy of delocalized states. One can ask to what extent the scaling of the splitting magnitude with the coupling strength is universal.

We would like to emphasize that the above scaling is not universal at all and depends strongly on the particular way of coupling of the CC networks. To support this statement, we return to Fig. 2. Suppose that direction of propagation in one of the subnetworks is reversed. Then, the model considered in this paper transforms into the random-magnetic-field network studied in Refs. 44 and 45 with a dramatically different outcome. Namely, the latter network does not exhibit delocalization at all. This illustrates how different the splitting is in coupled networks that are *copropagating* or *counterpropagating*. By translating into physical terms, the two transitions at $q - 1/2 = \pm p^{1/\gamma}$ in our model can be viewed as splitting of magnetic fields B and $-B$ for a *given* energy, at which two delocalization transitions take place. This is certainly different from the splitting of energies of delocalized states in a given magnetic field, described by the copropagating networks of Refs. 44 and 45.

Even if two networks are counterpropagating, differences in the details of coupling leads to different scaling of splitting. As an example, we refer to Ref. 68. It differs from our model in the structure of scattering matrices both at the link and nodes. As a result of these differences, the model in Ref. 68 possesses a metallic phase.

E. Phases with higher σ_{xy}

In fact, scaling theory predicts that *all* Landau levels n in Eq. (4) eventually levitate to $E_n \to \infty$, as the magnetic field is lowered. Our simulations do not capture low-field transitions for $n \geqslant 1$. This is because we restricted our consideration to a network with one channel per link. Within this description, we were able to capture the Drude conductivity tensor of electron gas in a weak field and weak localization effects. On the other hand, this description does not allow us, in principle, to capture the phases with quantized σ_{xy} higher than 1.

As a final remark, we can underscore the difference of the scaling theory and our results as follows. The scaling theory predicts that electron gas experiences a delocalization transition in a magnetic field at which flux into the area l^2 is of the order of the flux quantum Φ_0. We find that, in the limit of $k_F l > 10$, the interplay of orbital and phase actions of magnetic field causes the transition when this flux is much larger than Φ_0.

ACKNOWLEDGMENTS

We acknowledge the hospitality of KITP, Santa Barbara, where this project was initiated. V.V.M. and M.E.R. acknowledge the support of the DOE Grant No. DE-FG02-06ER46313 and BSF Grant No. 2006201, and useful discussions with I. Gruzberg and V. Kagalovsky. M.O. and A.M.S. are grateful for financial support from Spanish DGI Grant No. FIS2009-13483, and from Fundacion Seneca Grant No. 08832/PI/08.

[1]E. Abrahams, P. W. Anderson, D. C. Licciardello, and T. V. Ramakrishnan, Phys. Rev. Lett. **42**, 673 (1979).
[2]A. M. M. Pruisken, Nucl. Phys. B **235**, 277 (1984); A. M. M. Pruisken and I. S. Burmistrov, Ann. Phys. (NY) **316**, 285 (2005).
[3]D. E. Khmelnitskii, Phys. Lett. A **106**, 182 (1984); his prediction of levitation was based on analysis of RG flows, which he introduced earlier in Pis'ma v ZhETF **38**, 454 (1983) [JETP Lett. **38**, 552 (1983)].
[4]R. B. Laughlin, Phys. Rev. Lett. **52**, 2304 (1984).
[5]H. W. Jiang, C. E. Johnson, and K. L. Wang, Phys. Rev. B **46**, 12830 (1992).
[6]C. E. Johnson and H. W. Jiang, Phys. Rev. B **48**, 2823 (1993).
[7]H. W. Jiang, C. E. Johnson, K. L. Wang, and S. T. Hannahs, Phys. Rev. Lett. **71**, 1439 (1993).
[8]I. Glozman, C. E. Johnson, and H. W. Jiang, Phys. Rev. Lett. **74**, 594 (1995).
[9]I. Glozman, C. E. Johnson, and H. W. Jiang, Phys. Rev. B **52**, R14348 (1995).
[10]T. Wang, K. P. Clark, G. F. Spencer, A. M. Mack, and W. P. Kirk, Phys. Rev. Lett. **72**, 709 (1994).
[11]R. J. F. Hughes, J. T. Nicholls, J. E. F. Frost, E. H. Linfield, M. Pepper, C. J. B. Ford, D. A. Ritchie, G. A. C. Jones, E. Kogan, and M. Kaveh, J. Phys. Condens. Matter **6**, 4763 (1994).
[12]S.-H. Song, D. Shahar, D. C. Tsui, Y. H. Xie, and D. Monroe, Phys. Rev. Lett. **78**, 2200 (1997).
[13]D. Z. Liu, X. C. Xie, and Q. Niu, Phys. Rev. Lett. **76**, 975 (1996).
[14]K. Yang and R. N. Bhatt, Phys. Rev. Lett. **76**, 1316 (1996).
[15]D. N. Sheng and Z. Y. Weng, Phys. Rev. Lett. **78**, 318 (1997).
[16]D. N. Sheng and Z. Y. Weng, Phys. Rev. Lett. **80**, 580 (1998).
[17]D. N. Sheng and Z. Y. Weng, Phys. Rev. B **62**, 15363 (2000).
[18]Th. Koschny, H. Potempa, and L. Schweitzer, Phys. Rev. Lett. **86**, 3863 (2001).
[19]D. N. Sheng, Z. Y. Weng, and X. G. Wen, Phys. Rev. B **64**, 165317 (2001).
[20]X. Wan and R. N. Bhatt, Phys. Rev. B **64**, 201313 (2001).
[21]Th. Koschny and L. Schweitzer, Phys. Rev. B **70**, 165301 (2004).
[22]B. Huckestein, Phys. Rev. Lett. **84**, 3141 (2000).
[23]T. V. Shahbazyan and M. E. Raikh, Phys. Rev. Lett. **75**, 304 (1995).
[24]V. Kagalovsky, B. Horovitz, and Y. Avishai, Phys. Rev. B **52**, R17044 (1995).
[25]V. Kagalovsky, B. Horovitz, and Y. Avishai, Phys. Rev. B **55**, 7761 (1997).
[26]A. Gramada and M. E. Raikh, Phys. Rev. B **54**, 1928 (1996).
[27]F. D. M. Haldane and K. Yang, Phys. Rev. Lett. **78**, 298 (1997).
[28]M. M. Fogler, Phys. Rev. B **57**, 11947 (1998).
[29]A. L. C. Pereira and P. A. Schulz, Phys. Rev. B **66**, 155323 (2002).
[30]D. J. Thouless, M. Kohmoto, M. P. Nightingale, and M. den Nijs, Phys. Rev. Lett. **49**, 405 (1982).
[31]V. V. Mkhitaryan, V. Kagalovsky, and M. E. Raikh, Phys. Rev. Lett. **103**, 066801 (2009); Phys. Rev. B **81**, 165426 (2010).
[32]J. K. Jain, Phys. Rev. Lett. **63**, 199 (1989); Phys. Rev. B **40**, 8079 (1989); **41**, 7653 (1990).
[33]B. I. Halperin, P. A. Lee, and N. Read, Phys. Rev. B **47**, 7312 (1993).
[34]A. K. Geim, S. V. Dubonos, and A. V. Khaetskii, Pis'ma v ZhETF **51**, 107 (1990) [JETP Lett. **51**, 121 (1990)].
[35]S. J. Bending, K. von Klitzing, and K. Ploog, Phys. Rev. Lett. **65**, 1060 (1990).
[36]A. K. Geim, S. J. Bending, and I. V. Grigorieva, Phys. Rev. Lett. **69**, 2252 (1992).
[37]A. K. Geim, S. J. Bending, I. V. Grigorieva, and M. G. Blamire, Phys. Rev. B **49**, 5749 (1994).
[38]A. Smith, R. Taboryski, L. T. Hansen, C. B. Sørensen, Per Hedegård, and P. E. Lindelof, Phys. Rev. B **50**, 14726 (1994).
[39]F. B. Mancoff, R. M. Clarke, C. M. Marcus, S. C. Zhang, K. Campman, and A. C. Gossard, Phys. Rev. B **51**, 13269 (1995).
[40]G. M. Gusev, U. Gennser, X. Kleber, D. K. Maude, J. C. Portal, D. I. Lubyshev, P. Basmaji, M. de P. A. Silva, J. C. Rossi, and Yu. V. Nastaushev, Phys. Rev. B **53**, 13641 (1996).
[41]A. A. Bykov, G. M. Gusev, J. R. Leite, A. K. Bakarov, N. T. Moshegov, M. Cassé, D. K. Maude, and J. C. Portal, Phys. Rev. B **61**, 5505 (2000).
[42]A. W. Rushforth, B. L. Gallagher, P. C. Main, A. C. Neumann, M. Henini, C. H. Marrows, and B. J. Hickey, Phys. Rev. B **70**, 193313 (2004).
[43]A. G. Aronov, A. D. Mirlin, and P. Wölfle, Phys. Rev. B **49**, 16609 (1994).
[44]D. K. K. Lee and J. T. Chalker, Phys. Rev. Lett. **72**, 1510 (1994).
[45]D. K. K. Lee, J. T. Chalker, and D. Y. K. Ko, Phys. Rev. B **50**, 5272 (1994).
[46]D. B. Chklovskii and P. A. Lee, Phys. Rev. B **48**, 18060 (1993).
[47]D. B. Chklovskii, Phys. Rev. B **51**, 9895 (1995).

[48]V. I. Fal'ko, Phys. Rev. B **50**, 17406 (1994).
[49]D. V. Khveshchenko, Phys. Rev. Lett. **77**, 1817 (1996).
[50]A. D. Mirlin, D. G. Polyakov, and P. Wölfle, Phys. Rev. Lett. **80**, 2429 (1998).
[51]A. D. Mirlin, J. Wilke, F. Evers, D. G. Polyakov, and P. Wölfle, Phys. Rev. Lett. **83**, 2801 (1999).
[52]A. D. Mirlin, D. G. Polyakov, F. Evers, and P. Wölfle, Phys. Rev. Lett. **87**, 126805 (2001).
[53]A. V. Izyumov and B. D. Simons, J. Phys. A: Math. Gen. **32**, 5563 (1999).
[54]A. Shelankov, Phys. Rev. B **62**, 3196 (2000).
[55]H. Mathur and H. U. Baranger, Phys. Rev. B **64**, 235325 (2001).
[56]K. B. Efetov and V. R. Kogan, Phys. Rev. B **70**, 195326 (2004).
[57]D. G. Ravenhall, H. W. Wyld, and R. L. Schult, Phys. Rev. Lett. **62**, 1780 (1989).
[58]H. U. Baranger and A. D. Stone, Phys. Rev. Lett. **63**, 414 (1989).
[59]C. W. J. Beenakker and H. van Houten, Phys. Rev. Lett. **63**, 1857 (1989).
[60]J. T. Chalker and P. D. Coddington, J. Phys. C: Solid State Phys. **21**, 2665 (1988).
[61]D.-H. Lee, Z. Wang, and S. Kivelson, Phys. Rev. Lett. **70**, 4130 (1993).
[62]J. T. Chalker, M. Ortuño, and A. M. Somoza, Phys. Rev. B **83**, 115317 (2011).
[63]J. L. Cardy, J. Phys. A: Math. Gen. **35**, L565 (2002).
[64]V. Kagalovsky, B. Horovitz, Y. Avishai, and J. T. Chalker, Phys. Rev. Lett. **82**, 3516 (1999).
[65]M. Ortuño, A. M. Somoza, and J. T. Chalker, Phys. Rev. Lett. **102**, 070603 (2009).
[66]I. A. Gruzberg, A. W. W. Ludwig, and N. Read, Phys. Rev. Lett. **82**, 4524 (1999).
[67]E. J. Beamond, J. Cardy, and J. T. Chalker, Phys. Rev. B **65**, 214301 (2002).
[68]M. Bocquet and J. T. Chalker, Phys. Rev. B **67**, 054204 (2003).